C: Physical Processes in Nanomaterials and Nanostructures

# Effects of Zn Substitution in the Magnetic and Morphological Properties of Fe-Oxide Based Core-Shell Nanoparticles Produced in a Single Chemical Synthesis

Javier Lohr, Adriele Aparecida De Almeida, M. Sergio Moreno, Horacio E. Troiani, Gerardo F. Goya, Teobaldo Enrique Torres Molina, Rodrigo Fernandez-Pacheco, Elin L Winkler, Marcelo Vasquez Mansilla, Renato Cohen, Luiz C.C.M. Nagamine, Luis M. Rodriguez, Daniel E. Fregenal, Roberto D Zysler, and Enio Lima

*J. Phys. Chem. C*, **Just Accepted Manuscript** • DOI: 10.1021/acs.jpcc.8b08988 • Publication Date (Web): 20 Dec 2018

# Effects of Zn Substitution in the Magnetic and Morphological Properties of Fe-Oxide Based Core-Shell Nanoparticles Produced in a Single Chemical Synthesis

Javier Lohr[1], Adriele Aparecida de Almeida[1,2], M. Sergio Moreno[1], Horacio Troiani[2,3], Gerardo F. Goya[4,5], Teobaldo Enrique Torres Molina[5], Rodrigo Fernandez-Pacheco[5], Elin L. Winkler[1,2], Marcelo Vasquez Mansilla[1], Renato Cohen[6], Luiz C. C. M. Nagamine[6], Luis M. Rodríguez[1], Daniel E. Fregenal[1], Roberto D. Zysler[1,2], Enio Lima Jr.[1,*]

1 Instituto de Nanociencia y Nanotecnología CNEA-CONICET, Centro Atómico Bariloche, Av. Bustillo 9500, 8400 San Carlos de Bariloche, Argentina.

2 Instituto Balseiro, Universidad Nacional de Cuyo – CNEA, Av. Bustillo 9500, 8400 San Carlos de Bariloche, Argentina.

3 Laboratorio de Caracterización de Materiales y Óxidos No-Estequiometricos. Gerencia de Investigación Aplicada-CONICET.

4 Departamento de Física de la Materia Condensada, Facultad de Ciencias, Universidad de Zaragoza, 50009 Zaragoza, Spain.

5 Instituto de Nanociencia de Aragón (INA), Universidad de Zaragoza, 50018 Zaragoza, Spain.

6 Instituto de Física, Universidade de São Paulo, 05508-090 São Paulo, Brazil

* Corresponding author: lima@cab.cnea.gov.ar

**Abstract:**

Magnetic, compositional and morphological properties of Zn-Fe-oxide core-shell bimagnetic nanoparticles (MNPs) were studied for three samples with 0.00, 0.06 and 0.10 Zn/Fe ratios, as obtained from Particle-Induced X-ray Emission analysis. The bimagnetic nanoparticles were produced in one step synthesis by the thermal decomposition of the respective acetylacetonates. The nanoparticles present an average particle size between 25 - 30 nm as inferred from Transmission Electron Microscopy (TEM). High-Resolution TEM images clearly show core-shell morphology for the particles in all samples. The core is composed by an antiferromagnetic (AFM) phase with Wüstite ($Fe_{1-y}O$) structure, while the shell is composed by $Zn_xFe_{3-x}O_4$ ferrimagnetic (FiM) spinel phase. Despite the low solubility of the Zn in the Wüstite, Electron energy-loss spectroscopy (EELS) analysis indicates that the Zn is distributed almost homogeneously in the whole nanoparticle. This result gives information on the formation mechanisms of the particle, indicating that the Wüstite is formed firstly, and the superficial oxidation results in the FiM ferrite phase with similar Zn concentration than the core. Magnetization and in-field Mössbauer spectroscopy of the Zn-richest nanoparticles indicate that the AFM phase is strongly coupled to the FiM structure of the ferrite shell, resulting in a bias field ($H_{EB}$) appearing below $T_N^{FeO}$, with $H_{EB}$ values that depends on the core-shell relative proportion. Magnetic characterization also indicates a strong magnetic frustration for the samples with higher Zn concentration, even at low temperatures.

## INTRODUCTION

In the early 2000´s, the groups of Sun[1,2] and Hyeon[3,4] reported the synthesis of magnetic ferrite nanoparticles by thermal decomposition at relatively high temperatures (about 540-640 K) of organo-metallic precursors in the presence of surfactants and a long-chain alcohol. This method becomes a hit since it produces magnetic nanoparticles with several advantages with respect to others[5], such as a narrow size distribution and a high crystallinity, both critical for homogeneous magnetic properties, and simultaneously it allows an easy way to control stoichiometry[2]. The success of this method is based in a well separately nucleation and growth/crystallization process that take place at different temperatures[6], being extensively used to synthesize magnetic nanoparticles[7-12].

An interesting feature was reported on the fundamentals of the thermal decomposition method by Hao et al in 2007[13]: a massive reduction of iron ions in the synthesis solution, leading to the formation of nanoparticle with diameter larger than 14 nm containing the antiferromagnetic Wüstite phase ($Fe_{1-y}O$), which is followed by the oxidation and consequent formation of a ferrimagnetic (FiM) ferrite phase ($Fe_3O_4$ or $\gamma$-$Fe_2O_3$). The result was a bimagnetic core-shell nanoparticle produced in a one-pot reaction, with an antiferromagnetic (AFM) core ($Fe_{1-y}O$) below $T_N$ = 198 K[14] and a FiM shell. In fact, in the work of Hyeon et al in 2004[3], it is possible to observe remarkable features around 200 K in the ZFC Magnetization *vs.* Temperature curves for large particles (d > 16 nm) that could be related to Néel temperature ($T_N$) of the AFM phase. When the formation of $Fe_{1-y}O$ phase took place during the synthesis, the presence of the AFM phase is expected for larger particles since the oxidation to the FiM phase could not be complete, keeping an AFM core. Other works report on the formation of $Fe_{1-y}O$ and a ferrite phase in a core-shell structure after oxidation by the thermal decomposition method[15-19]. As pointed out by Chen et al[20], the Wüstite phase is formed as consequence of reactions involving some commonly used hydrocarbon solvents and its formation contributes to significant cationic disorder. The later formation of the bimagnetic core-shell system due to the surface oxidation of Wüstite results in very distinct magnetic properties with respect to the monophasic nanoparticles[21-26]. Therefore, it is very important determine the factors that govern the core/shell nanoparticles formation to establish the reproducibility of this synthesis method and the magnetic response of the system. Different magnetic ions present different degree of

solubility in the Wüstite phase. While Chen et al[27] have determined a relatively homogeneous distribution of Co ions along the entire particle, including core (Wüstite) and shell (ferrite) and similar observation was found for the Mn ions[28] and also for the diamagnetic $Mg^{2+}$ ion[29-31]; the $Zn^{2+}$ ions present low solubility in the Wüstite with an upper limit of approximately 10 %[32]. This result can lead to a stoichiometric heterogeneity when the formation of $Fe_{1-y}O$ takes place with important consequences in the magnetic response of the system. As the production of iron oxides nanoparticles doped with Zn is of great current interest due to the surface chemistry of the system as well its magnetic response for bio-application and innovative technologies[33-36], it is crucial determine the role of the different parameter that establish the morphology and magnetic properties of this system. With this premise, in this work we have produced by the thermal decomposition method Zn-$Fe_{1-y}O/Zn_xFe_{3-x}O_4$ bimagnetic core-shell nanoparticles and study its structural, morphology and magnetic properties. We have analyzed the effect of the low solubility of the Zn in the Wüstite in the composition homogeneity and its effects on the nanoparticles physical properties.

## EXPERIMENTAL PROCEDURE

*Sample Preparation*

Three sample with distinct Zn amounts in the composition were prepared by the thermal decomposition of the $Fe^{3+}$ acetylacetonate ($Fe(C_5H_7O_2)_3$ – $Fe(acac)_3$ - Aldrich 97%) and $Zn^{2+}$ acetylacetonate ($Zn(C_5H_7O_2)_2 \cdot xH_2O$ – $Zn(acac)_2$ – Aldrich, with estimation of 20 % wt. of water as obtained from DTA-TGA measurements). Samples were labeled according with the Zn/Fe relation determined by Particle-Induced X-ray Emission (PIXE) analysis (z = $[Zn]_{PIXE}/[Fe]_{PIXE}$): z = 0.10, z = 0.06, z = 0.00. For sample z = 0.00, a total of 5.7 mM of $Fe(acac)_3$ were dispersed in 50 mL of octadecene ($CH_3(CH_2)_{15}CH=CH_2$ – Aldrich 90 %) with 56.6 mM of Oleic acid ($CH_3(CH_2)_7CH=CH(CH_2)_7COOH$ - PanReac, PharmaGrade), 56.6 mM of oleylamine ($CH_3(CH_2)_7CH=CH(CH2)_7CH_2NH_2$ – Aldrich 70%) and 5.7 mM of 1,2-octanediol ($CH_3(CH_2)_5CH(OH)CH_2OH$ – Aldrich 98%). Sample z = 0.06 was prepared with 4.5 mM of $Fe(acac)_3$ and 0.5 mM of $Zn(acac)_2$ dispersed in 50 mL of octadecene and adding 26 mM of Oleic acid, 26 mM of oleylamine and 3.5 mM of 1,2-

octanediol. Sample z = 0.10 was prepared using 4.6 mM of $Fe(acac)_3$ and 1.1 mM of $Zn(acac)_2$ dispersed in 50 mL of trioctylamine ($[CH_3(CH_2)_7]_3N$ – Aldrich 98 %) and 22.5 mM of oleic acid. For all samples, a 3-neck flask was used with one neck for the $N_2$ (White Martins - 5.0) flux, other for a mechanical stirring (the central one) and the third one for a condenser. The synthesis solution of all samples were mechanically stirred at room temperature, heated to 373-393 K during 30 minutes with a $N_2$ flux of 0.5 mL/min, without the presence of condenser in order to remove humidity of the system. After that, the system was closed with the condenser keeping the $N_2$ flux, and the solution was heated up to 473 K with a controlled increment of temperature (about 3 K/min.). The solution was kept in this temperature about 5 minutes and then it was heated up to the reflux condition with a heating ramp of ~20 K/min: 610-615 K for octadecene and 630-635 K for trioctylamine. After that, the heating source was removed in order to get a rapid cooling of the solution. At 313 K, the flask is opened and 400 mL of Ethanol (96 % - Porta) is added in order to precipitate the particles. Finally, a solution of Ethanol and Acetone (99.9 % - Sigma-Aldrich) (about 10:1, respectively) was added on the particles followed by centrifugation at 14000 rpm for 30 minutes. A second cleaning only with acetone is performed, also followed by centrifugation. The final product, the as-made sample, is a powder containing hydrophobic nanoparticles coated with an organic layer of oleic acid.

A differential thermal thermogravimetric analyzer (TGA) Schimadzu DTG-60H was used to determinate the percentage of organic compound in the as-made nanoparticles to have accuracy in the mass determination to normalize magnetization experimental data with the oxide amount. For this, each as-made powder sample was heating up to 1173 K with a heating rate of 3 K/min in Ar flux (100 mL/min) while the weight loss was measured, which corresponds to the amount of organic compound in nanoparticles. This technique also was used to determine the amount of water in the $Zn(acac)_2$, where the reagent was heated up to 453 K with a heating rate of 3 K/min in Ar flux (100 mL/min).

Structural characterization was carried out using a PANalytical Empyrean powder X-ray diffractometer ($CuK_\alpha$, $\lambda$=0.15418 nm). Samples were cleaning with acetone, to remove organic material and a zero diffraction plate holder was used in measurement.

Transmission Electron Microscopy (TEM) images were carried out in two microscopies. For both microscopes, TEM specimens were prepared by dispersing the dried powdered

samples in isopropanol and dropping the solution onto a carbon covered grid. For TEM and High-Resolution TEM (HRTEM), the images were obtained with a Tecnai F20 G2 (ThermoFisher Scientific, formerly FEI) microscope operating at 200 kV at room temperature. The mean particle size (<D>) was determined after count ~300 particles and fitting the corresponding histogram with a lognormal distribution. For the Scanning Transmission Electron Microscopy - High Angle Annular Dark Field (STEM-HAADF), the images were obtained in a Cs-probe-corrected Titan (ThermoFisher Scientific, formerly FEI) at a working voltage of 300 KV, coupled with a HAADF detector (Fischione). The chemical composition of the nanoparticles was analyzed by Electron Energy Loss Spectroscopy (EELS), in order to obtain the concentration ratio Fe/Zn at the core and the shell. Low-loss EEL spectra were obtained with a Tridiem Energy Filter (Gatan) spectrometer. For every linescan, a 5 ms spectrum was obtained every 0.1 nm. The Energy dispersion used for the analysis was 0.1 eV/pixel. The collection semi-angle (Beta) was 32.6 mrad for a camera length of 10 mm and a spectrometer entrance aperture of 1 µm. The convergence semi-angle (Alpha) was 24.8 mrad for a condenser aperture of 70 µm. The energy resolution, estimated from the full width at half maximum of the zero-loss peak, was 1.4 eV.

Chemical composition of the nanoparticles was measured with Particle induced X-ray emission spectroscopy (PIXE) technique[37], with using a 3 MeV $H^+$ beam in a NEC 5SDH 1.7 MV tandem accelerator with a NEC RC43 end-station[38]. To prepare the nanoparticles samples they were properly washed and dried and then placed on the sample holder with carbon tape. PIXE spectra were analysed using GUPIX software[39].

Magnetization measurements as function of temperature (M(T)) and isothermal curves (T = 5 K) as function of applied field ($M_{5K}(H)$) were measured in a commercial Quantum Design MPMS-5S SQUID magnetometer. M(T) curves were measured applied field of 50 Oe in Zero Field Cooling (ZFC) and Field Cooling (FC) protocols. $M_{5K}(H)$ curves were measured in both conditions: after ZFC protocol and after a FC protocol. For the FC protocol, the sample was cooled from T = 300 K to 5 K (starting above the $T_N$ ~ 200 K of $Fe_{1-y}O$ AFM phase) with applied field of $H_{FC}$ = 50 kOe. Isothermal curves at T = 100 K ($M_{100K}(H)$) and 300 K ($M_{300K}(H)$) were measured in a LakeShore 7300 vibrating sample magnetometer (VSM). $M_{100K}(H)$ measurements were also performed in both ZFC and FC

protocols, with an applied field in the cooling procedure of $H_{FC}$ = 10 kOe. $M_{300K}(H)$ measurements were used in order to determine saturation magnetization ($M_S$) at room temperature. For all magnetic measurements, the samples were conditioned by dispersing the nanoparticles in toluene and paraffin, followed by the toluene evaporation, in order to avoid agglomeration and to immobilize them.

In-field Mössbauer spectra (MS) of sample z = 0.10 were taken at 4.2 K in a liquid He flow cryostat with a spectrometer in transmission geometry with using a $^{57}$Co/Rh source. The spectra were collected after a field cooling procedure with applied field of $H_{FC}$ = 120 kOe from 300 K (above $T_N$). Mössbauer samples were prepared by dispersing 20 mg of the respective powder samples in boron nitride and pressing it between acrylic discs. The sample was mounted in the bore of a 140 kOe superconducting magnet, in a vertical source-sample-detector setup such that the direction of gamma-ray was parallel to the direction of applied field. A sine-shaped velocity waveform was used to minimize mechanical noise. All MS spectra were fitted by using Lorentzian line shapes with non-linear least-square software, with calibrating the velocity scale with α-Fe foil at 300 K. Isomer shift values are relative to α-Fe at 300 K. As a consequence of the experimental setup, the temperature of the source during the low-temperature spectrum acquisition must be considered as an important factor to the isomer shift (IS) values observed in order to compare with the expected ones.

## RESULTS AND DISCUSSION

### *Morphology and Composition*

Figure 1 shows the measured PIXE spectra of all as-made samples and their corresponding fittings performed with GUPIX software. The procedure of fabrication and sample preparation involves the presence of extra elements, mainly carbon and oxygen due to the imponderable contribution from different sources, like carbon tape, solvent remains and contamination. Restricting us to the nanoparticles composition, just the Zn and Fe quantities are taking into the account using the peaks associated to the K-shell transitions. The value $z = [Zn]_{PIXE}/[Fe]_{PIXE}$ for each sample was used to label each sample in Table 1, with the corresponding uncertain in the parenthesis. The amount of Zn in samples z = 0.10 (2) and 0.06 (2) are lower than the expected from the molar relation of precursors

([$Zn(acac)_2$]/[$Fe(acac)_3$]) used in the synthesis procedure: 0.58 for sample z = 0.10 (2) and 0.30 for sample z = 0.06 (2). This result indicates that the incorporation of the Zn ions to the nanoparticles is limited in the synthesis procedure, probably as consequence of the low Zn solubility in the Wüstite phase.

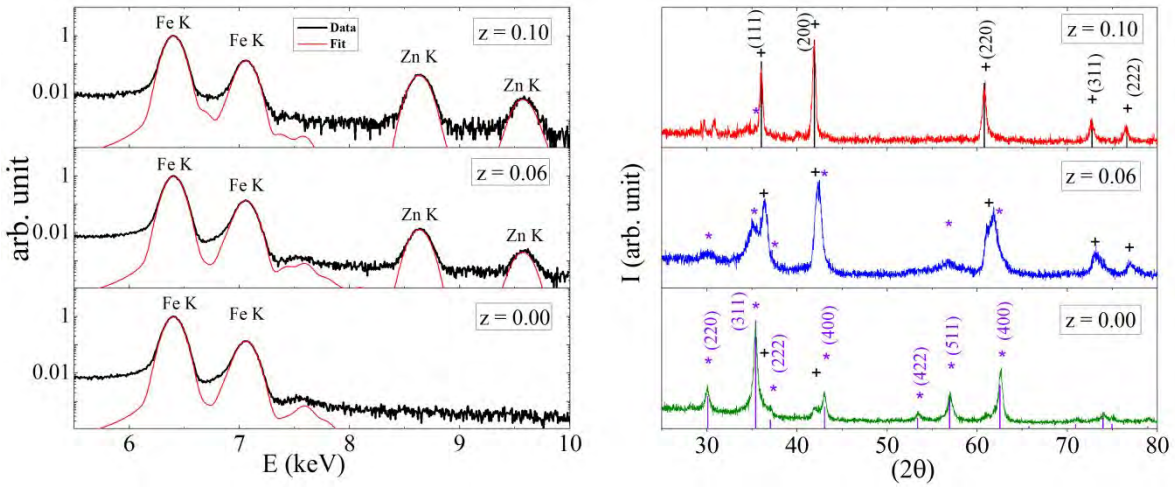


Figure 1 – Left Panel: PIXE spectra of all samples showing the pertinent energy range of Fe and Zn K-peaks. Black lines correspond to experimental data, and red lines are the respective fitting to obtain the z =[Zn]/[Fe] ratio for each system. Right panel: XRD profiles of three samples. All peaks are indexed with the $Fe_{1-y}O$ (+) and ferrite (*) phases where the bars correspond to the diffraction peaks according to the JCPDS card number: for Wüstite 00-006-0615 (upper panel) and magnetite 00-019-0629 (bottom panel).

Figure 1 also presents the XRD patterns of samples z = 0.10, 0.06 and 0.00. The diffraction pattern of sample with z = 0.10 mainly corresponds to the phase $Fe_{1-y}O$, despites some peaks of ferrite phase are observed with very low intensity. The peaks (111), (200) and (220) of $Fe_{1-y}O$ were fitted with a pseudo-voigt function in order to obtain the full width at half maximum (FWHM), then the crystallite size ($D_{XRD}$) was obtained by using the Scherrer's equation which results in the 20 nm-25 nm range. Instead the XRD profile of sample z = 0.06 clearly evidences the presence of ferrite structure together with the $Fe_{1-y}O$ phase, in almost similar amounts when considering the peak areas. From the Scherrer´s equation the $D_{XRD}$ were calculated for these phases, obtaining 7 nm for the reflection (311) of ferrite phase and 15 nm for the reflection (111) of $Fe_{1-y}O$ phase. Moreover, for sample z = 0.00, both phases are also observed, with a relation of Ferrite/$Fe_{1-y}O \approx 2/1$ obtained from

the respective peak´s area. The values of $D_{XRD}$ ≈12 nm and 21 nm were calculated from the reflection (200) of $Fe_{1-y}O$ phase and from the reflections (311) and (400) of the ferrite, respectively. The XRD analysis of the three samples shows that the proportion of Wüstite phase increases as the Zn concentration in the particles increases: from a predominant ferrite phase for sample z = 0.00 to the widely dominant Wüstite phase in sample z = 0.10, in concordance with the increment in the corresponding crystallite size $D_{XRD}$ of this phase.

Figure 2 shows representative TEM images at lower magnification of nanoparticles in samples z = 0.10, 0.06 and 0.00. The diameter histogram for each sample was build up by measuring the diameter of more than 300 nanoparticles, also presented in figure 2. The histograms were fitted with lognormal distribution and the mean diameters are 30 nm, 26 nm and 26 nm for samples z = 0.10, 0.06 and 0.00, respectively, with a dispersion of σ~0.2 nm. A core/shell structure is observed in TEM images even at low magnification. From TEM images at higher magnification, the shell thickness were measured and the relative volume of each component were calculated, obtaining the volume proportion for the shell ($\%V_{shell}$) of 55% for sample z = 0.10, 65% for z = 0.06 and 70% for z = 0.00, as given in Table 1. Figure 3a shows a representative HRTEM image of nanoparticle in z = 0.10, where the core/shell is clearly evidenced. The Fast Fourier Transform (FFT) of different zones in the same particle gives the reciprocal *d*-spacing of each morphological component (core and shell). The FFT (upper right panel) of shell zone (light Blue Square in HRTEM) shows exclusively a *d*-spacing corresponding to the planes (220) of ferrite, which is marked as a red solid line circle; any contribution of Wüstite is not expected in this d-spacing range. Other interplanar distances appear for a large zone inside the core (orange square in HRTEM): the reciprocal distances observed in this FFT image between the planes (220) and (400) of ferrite corresponds to a *d*-spacing referent to the plane (200) of Wüstite, which is indicated in the figure as the green dashed-line. Similar characteristics are observed for the HRTEM of z = 0.06 (figure 3b). The FFT of shell zone also shows spots corresponding to the (220) planes of ferrite (marked in figure as a red solid line), while the FFT of a large area taking core and shell of the particle present other distances: the red circles for (311) and (222) of ferrite and green dashed-line circle for (111) of Wüstite phase. Finally, similar results are also obtained from the HRTEM of z = 0.00 (figure 3c). The FFT in shell zone shows spots corresponding to (220) planes of ferrites (red on line) and the FFT of the core

shows family of planes: (111), (220), (311) and (222) (not marked in the figure) for ferrites and the reciprocal interplanar distance for (111) of Wüstite. Our result shows that sample z = 0.10 has a bigger core volume than the other samples, presenting a systematic increase of $\%V_{shell}$ with the Zn amount. Nevertheless, its increment in the core volume with the amount of Zn not necessarily can be an exclusive consequence of the amount of Zn in the sample or in the synthesis solution. Others small changes in the synthesis conditions, including the redox potential could be related to this change.

Figure 4 shows a representative STEM-HAADF image of the nanoparticles (left panel) corresponding to sample with z = 0.10. The linescan used for STEM SI is indicated. Two spectra corresponding to the shell and the center of the core were extracted at the positions indicated in the image and shown in the right panel. In the spectra the Fe-M edges are visible at about 60 eV. The Zn-M edges can be observed as a weak bump at about 84 eV. For the extraction of these edges an $AE^{-r}$ power law background was subtracted. The width of the energy window for typical background fit for Zn edge and the estimated background are indicated in the figure 4. The background subtracted Zn-M edges are shown. The Fe/Zn ratio obtained at both positions was the same for the range 8-9. This evaluation indicates that Zn is present over the whole volume of the nanoparticle and that the doping concentration is approximately the same in the core and in the shell.

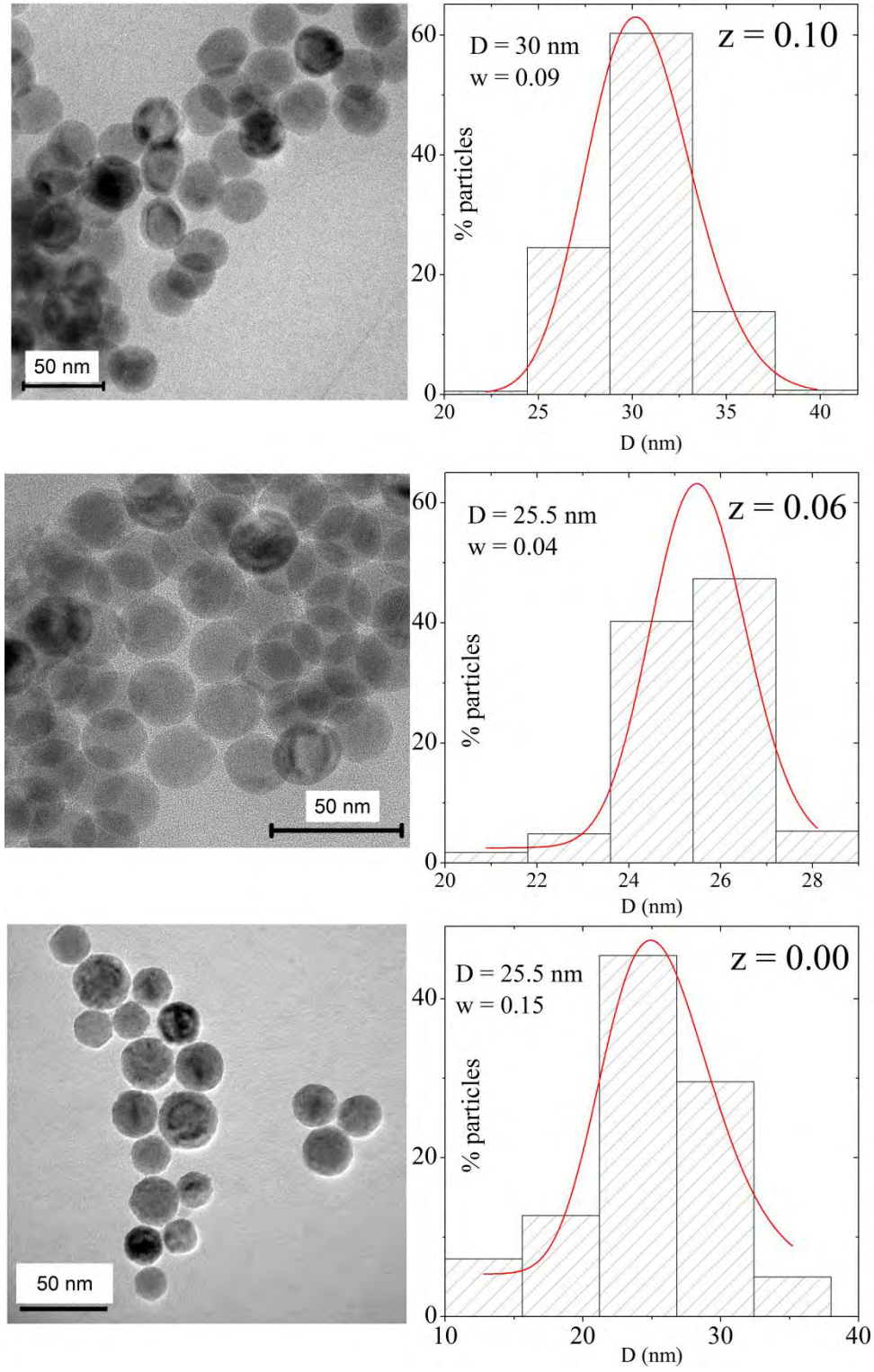


Figure 2 – Representative TEM image for each sample with the corresponding histogram of diameters obtained with measuring more than 300 particles. Each histogram is fitted with a lognormal distribution in order to obtain the mean diameter and the dispersion.

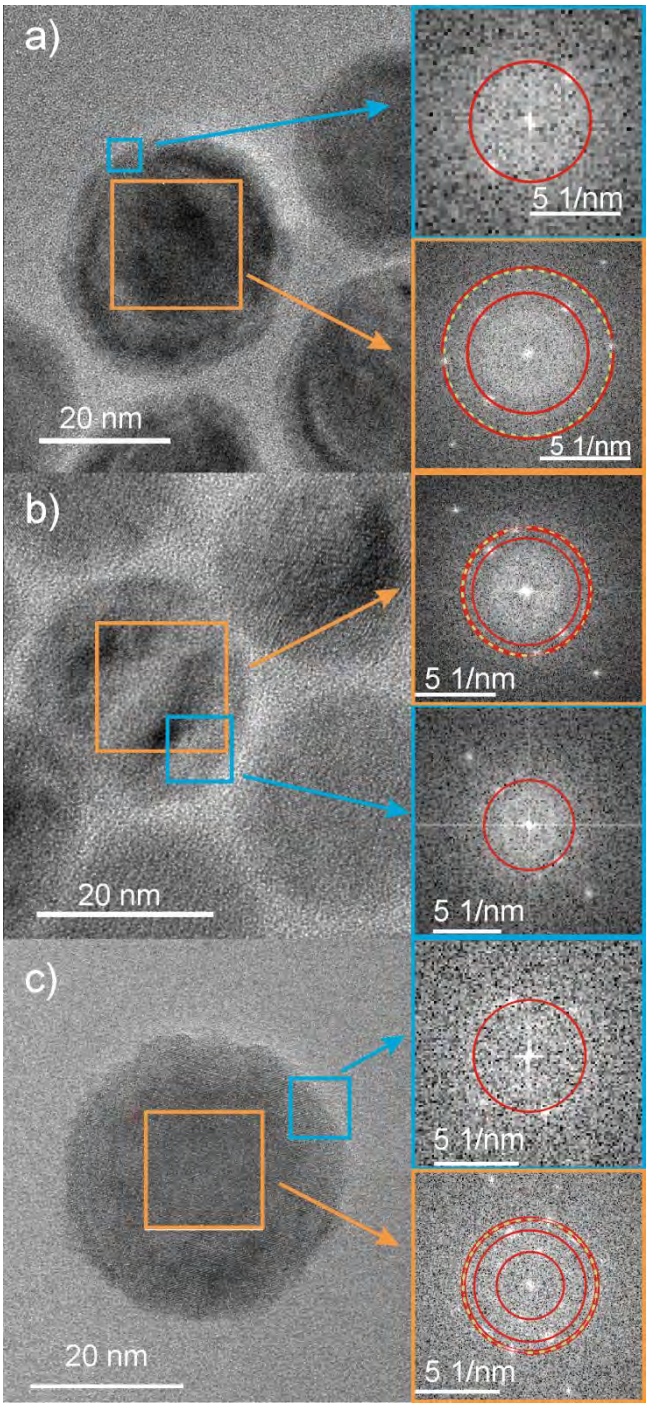


Figure 3 – Left panels show the HRTEM image of a representative nanoparticle of the sample with z = 0.10 (a), z = 0.06 (b) and z = 0.00 (c); right panels show the FFT from the zones marked with a square in the HRTEM image of the core (orange) and shell (blue), as indicated by the arrows. The FFT patterns of shell were indexed with the cubic spinel interplanar distances (solid red line), while the patterns of the core are indexed with cubic spinel and Wüstite (orange dashed line) interplanar distances.

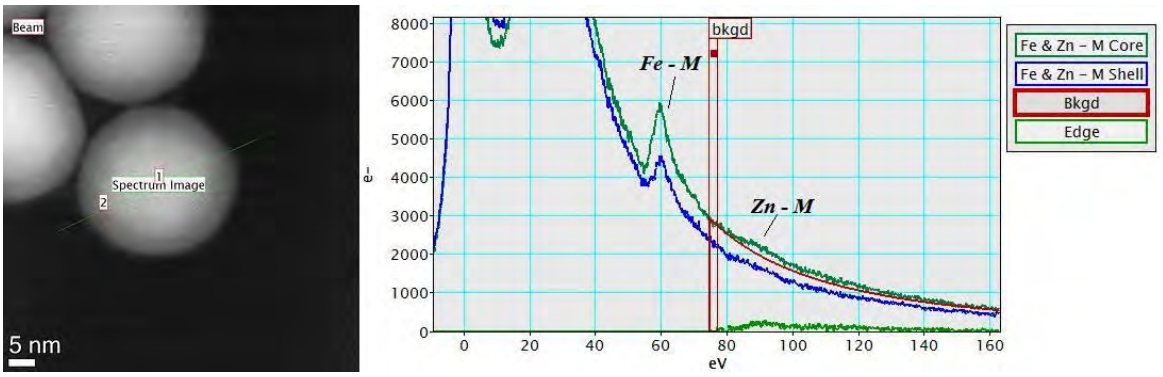


Figure 4 - STEM-HAADF image of nanoparticles of sample z = 0.10 (left) and low-loss EEL spectra (right) at different positions of the nanoparticle (indicated by 1 and 2 in the figure). The Fe-M and Zn-M edges are indicated. Background subtracted is indicated (red line). The background subtracted Zn-M edge is also shown.

Considering the morphological and compositional analyzes, we can obtain information about the growth mechanisms of the core-shell nanostructures. These results are consistent with the formation of the $Fe_{1-y}O$, at the initial stage of the synthesis followed by the formation of the ferrite phase as a consequence of the surface oxidation, which are in agreement with the PIXE analysis. This growth mechanism leads to the formation of well-defined interfaces, when they are compared with systems where the shell is growth in a second reaction[22,40], with the expectation of an improved magnetic exchange interaction between the phases. Other interesting feature is the reduction in the Zn incorporation in the formed material related to the nominal composition, which is probably related with the well-known low solubility of the Zn in the Wüstite structure mentioned before[32].

***Magnetic Properties***

M(T) curves of all samples measured in ZFC and FC protocols with $H$ = 50 Oe are presented in figure 5. The characteristic FC magnetization curves of nanoparticles of FiM material below the blocking temperature is a slightly increasing curve with a not so pronounced slope[41]. For our samples, a marked decrease in the magnetization in 175 K < $T$ < 210 K is observed for both ZFC and FC curves for all samples. This decrease is associated to the antiferromagnetic (AFM) ordering transition at the Néel temperature, $T_N$, of the Wüstite phase ($T_N$ values of all samples are presented in Table 1). For these range of

composition the AFM transition temperature does not show a significantly dependence with the Zn concentration. It is noteworthy that the decrease in the magnetization at $T_N$ is larger with increasing the Zn content, in concordance with the increasing proportion of the AFM Wüstite phase as revealed by the XRD and TEM analyzes. Notice that for sample z = 0.10, where the Wüstite is the main phase, a sharper AFM transition at $T_N$ is observed. Interestingly, irreversibility between ZFC and FC curves is observed below $T_N$. This irreversibility is ascribed to the magnetic behavior of the shell ferrimagnetic phase which is strongly magnetic coupled to the AFM core below $T_N$. Therefore, as expect for strongly FiM-soft/AFM-hard exchange coupled system, the blocking temperature shifts to the Néel temperature of the hard magnetic component.[21,23] Instead, for samples with z = 0.06 and z = 0.00, the irreversibility temperature is above $T_N$, indicating that there is a distribution of nanoparticles with blocking temperatures above $T_N$. This result could be the consequence of the larger proportion of FiM spinel shell phase as determined by TEM and XRD measurements and also to the lower concentration of Zn in the shell which lead to an increasing of the shell magnetic anisotropy. As a consequence the AFM transition in these sample is smoothed in comparison to that of sample z = 0.10.

The saturation magnetization of the samples was determined from the M(H) curves measured at T = 300 K. As observed in Table 1, $M_S$ decreases from 60 emu/g to 3 emu/g when the concentration of Zn increases. The huge reduction in $M_S$ for sample z = 0.10 comes mainly from the larger proportion of Wüstite phase, which is paramagnetic at room temperature. Besides, the larger substitution of Fe by Zn, plus the surface disorder driven by the thinner shell in this sample, could induce a strong spin-canting in the FiM shell, which reduces $M_S$ and the effective magnetic anisotropy K[42].

The zinc ferrite normal spinel shows AFM ordering below ~10 K; instead, in our partially substituted ferrite, FiM ordering is expected[43,44]. Although the $Zn^{2+}$ has tetrahedral site preference in the spinel structure, at nanometric scale some cationic inversion degree is observed. It is also well-known that the presence of Zn leads to spin-canting as resulting of its diamagnetic nature and the consequent lack of exchange coupling for the $Fe^{3+}$ and $Fe^{2+}$ in the neighborhood for Zn concentrations higher than 0.16[45]. In addition, spin canting is observed for systems as only consequence of the nanometric size[43,44], which should be increased in our system as consequence of the thickness of the ferrite phase shell estimated

of 5 nm for sample z = 0.10. Finally, a strong magnetic interaction between the FiM shell and the AFM core leads to the increment of uncompensated spins from the core and/or shell as well as to the increment of the magnetic canting in the shell phase[21,46]. Thus, the low magnetization values for high field observed for sample z = 0.10 probably reflects the nanometric core-shell magnetically coupled nature of the nanoparticles together with the partial substitution of Fe ion by Zn ions in the shell.

The hysteresis curves at T = 5 K and T = 100 K were measured by using two different protocols (Figure 5 right panel): after cooling from 300 K without (ZFC) and with an applied magnetic field of 50 kOe (FC). Remarkable, in the FC mode all samples shows large exchange bias fields ($H_{bias}$). The presence of $H_{bias}$ indicates a strong magnetic coupling between the AFM and the FiM phases, supporting the same conclusion observed in M(T) curves where an increases of the blocking temperature of the shell to the AFM ordering transition temperature of the core was observed. Sample z = 0.10 presents the larger exchange bias field where at 5 K results $H_{bias}^{5K} \sim 3420$ Oe. However, the FC cycle measured up to 5 T corresponds to a minor cycle; and larger $H_{bias}^{5K}$ is expected for higher applied fields. Sample z = 0.06 presents a totally saturated magnetization loop at 5 K, besides the $M_S$ as well the $H_C$ measured from the FC cycle are larger than the ones obtained from the ZFC measurement. This results is a consequence of the magnetic coupling at the AFM/FiM interface, where the FC protocol preferentially orient the AFM surface spins, and as a consequence enhance the coercivity and also the saturation magnetization. As expected the sample with z = 0.00 presents the lower $H_{bias}^{5K}$ (86 Oe), and the largest value of $M_S$, since it has the smallest AFM phase proportion.

Table1: Nanoparticles characteristic obtained from TEM, M(T) and M(H) measurements: $\%V_{shell}$ is the volume percentage of shell as calculated from the shell thickness and core diameter from TEM images, $M_S$ is the saturation magnetization at room temperature, $T_N$ is the Néel temperature, $H_{bias}^{5K}$ and $H_{bias}^{100K}$ are the exchange bias fields and $H_C^{5K}$ and $H_C^{100K}$ are the coercive fields, obtained from $M_{FC}(H)$ curves at 5 K and 100 K, respectively.

| Sample | $\%V_{shell}$ (%) | $M_s$ (emu/g) | $T_N$ (K) | $H_{bias}^{5K}$ (Oe) | $H_C^{5K}$ (Oe) | $H_{bias}^{100K}$ (Oe) | $H_C^{100K}$ (Oe) |
|---|---|---|---|---|---|---|---|
| *z*=0.00 | 70 | 59.6 | 196 | 86 | 30 | 30 | 454 |

| | | | | | | | |
|---|---|---|---|---|---|---|---|
| *z*=0.06 (2) | 65 | 16.8 | 180 | 2270 | 3580 | 435 | 673 |
| *z*=0.10 (2) | 55 | 3.2 | 177 | 3420 | 6150 | 429 | 276 |

Although in ideal AFM/FiM exchange coupled system it is predicted that the exchange bias properties should be present up to $T_N$; in core/shell nanoparticles, as a consequence of finite size effect and surface imperfections, it is usually observed that the exchange bias field vanish at much lower temperature.[22] In the present system the measurements performed at 100 K also present exchange bias field ($H_{bias}^{100K}$), indicating a good magnetic coupling through the interface; in fact, the exchange bias was observed up to 150 K for sample z = 0.10, close to the ordering temperature of the AFM phase. Figure 6 compares the variation of $H_{bias}^{5K}$ and $H_{bias}^{100K}$ with the Zn concentration. As expected, $H_{bias}^{5K}$ and also $H_C^{5K}$ increases with the Zn amount because the diameter of the AFM core grows and consequently the magnetic anisotropy of the AFM phase increases relatively to the other concentration. Instead, at higher temperature $H_{bias}^{100K}$ and $H_C^{100K}$ do not follow a monotonous dependence with the concentration. We ascribed this behavior to the thermal fluctuations, which are more important when the anisotropy is reduced as a consequence of the Zn incorporation in the structure. In summary, the overall magnetic measurements indicates that the nanoparticles cores are composed by the AFM phase with Wüstite structure while the shell presents a FiM ordering, both phase are strongly coupled below $T_N$ even at temperature higher than 100 K and finally the properties of the ferrite phase in the shell differ from those of magnetite or maghemita as a consequence of the coupling and the surface disorder.

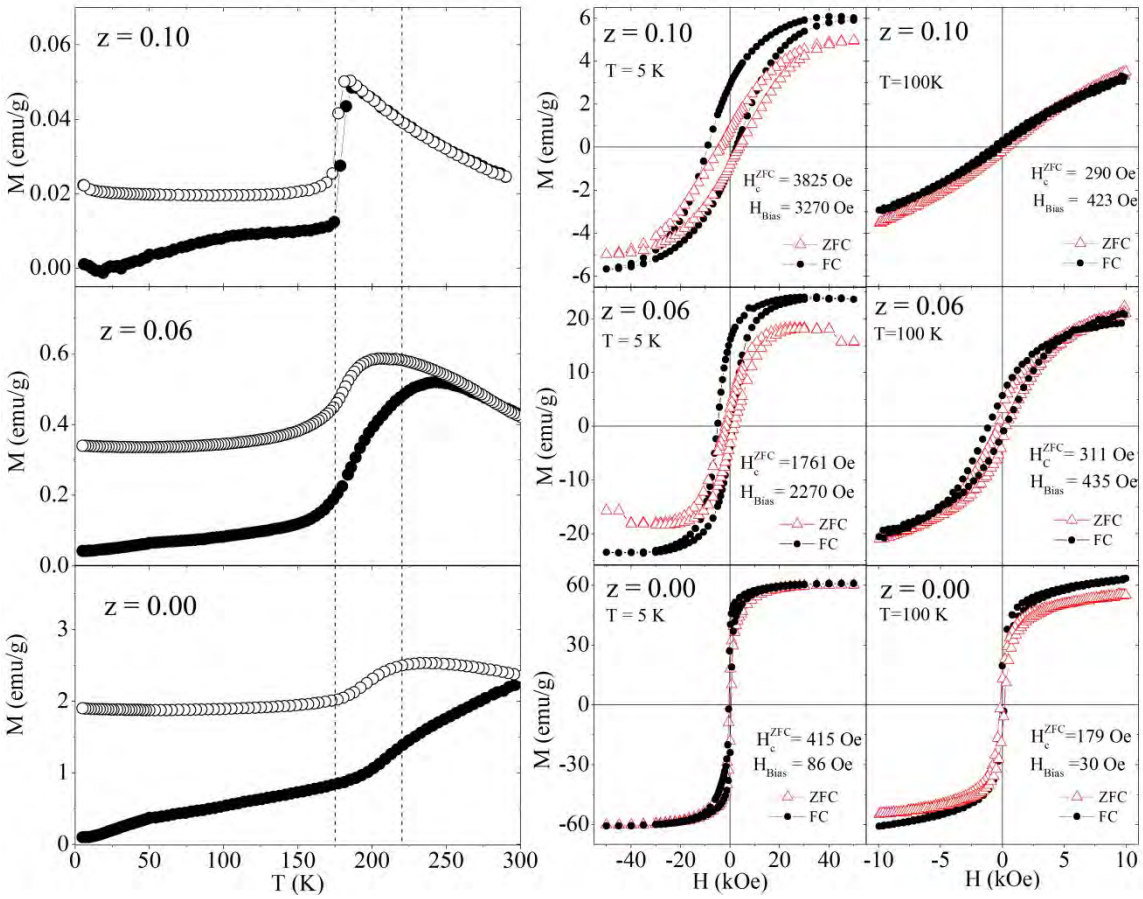


Figure 5 – Left panel: M(T) data of all samples measured in both ZFC (solid symbols) and FC (open symbols) protocols with $H_{FC}$=50 Oe. Right panel: ZFC (open symbols) and FC (solid symbols) hysteresis loops measured at 5 K (left panels) and 100 K (right panels). The values of coercive fields after ZFC ($H_C^{ZFC}$) and bias fields after FC defined as $H_{Bias}=(H_C^{+}-H_C^{-})/2$) are also displayed.

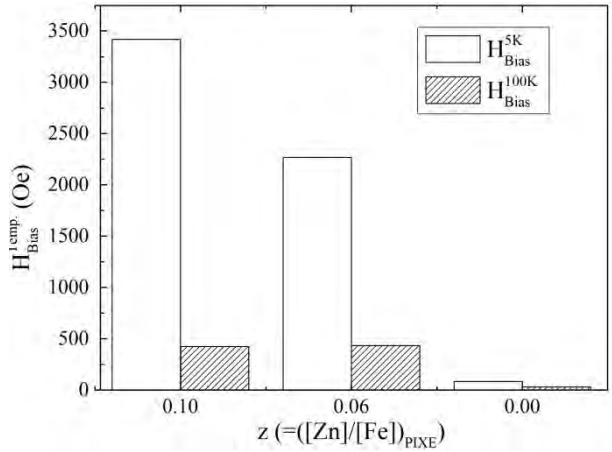

Figure 6 - Exchange bias field at 5 K ($H_{bias}^{5K}$) and 100 K ($H_{bias}^{100K}$) as a function of the Zn concentration of the sample obtained from PIXE analysis.

***In-Field Mössbauer Spectroscopy***

In order to get local information about the magnetic arrangement with the presence of the Zn in the bi-magnetic core-shell structure, in-field Mössbauer Spectroscopy was performed for sample z = 0.10. The spectra are given in figure 7 and they were collected with different applied fields. The spectra were fitted with two crystalline sextets, labeled sextets 1 and 2, a singlet probably related to $Fe^{3+}$ ions in the tetrahedral interstitial sites of Wüstite structure[18,47,48] and sextet with broad lines and lower effective field ($\overrightarrow{B_{eff}} = \overrightarrow{B_{hyp}} + \overrightarrow{B_{app,}}$ and $\overrightarrow{B_{hyp}}$ is the hyperfine field), labeled sextet 3. The linewidth was hold between the widths of the 6 lines of sextet: $\Gamma_{3,4}$=W+0.02526*dW, $\Gamma_{2,5}$=W+0.09344*dW, $\Gamma_{1,6}$=W+0.16147*dW. This can be shown to result from a relatively narrow effective field distribution, such as can often be seen in ferrites. All hyperfine parameters obtained from the fitting procedure are given in Table 2. For applied field from 0 to 120 kOe, the hyperfine field of the sextets 1 and 2, those with larger $B_{eff}$ increase and decrease, respectively, with the applied field as expected for a strong antiferromagnetic alignment, specifically for a FiM ordering as the subspectra areas are different with a relative relation of 1:1.6. These sextets could be easily referred to the two AFM aligned magnetic sub-lattices of the ferrite[49,50] consistent with the absence of the Verwey transition and in an opposition to the five sextets of the magnetite below the Verwey transition[47]. Nevertheless, as the Zn ions are known to occupy preferentially the A site in the ferrite structure, we expect an increase in this relation from 1.67 or 2 (maghemite or magnetite), not the observed decrease. In another way, if we consider a strong coupling among both sites, with the AFM ordering in the phase with structure of Wüsstite aligned with the A and B magnetic lattice of the ferrite, and considering presence of 10 % of Zn in the A site of the ferrite structure and the amounts of each phase as obtained from the volume estimated from HRTEM images, then a relation of areas about 1.60 between both sites is expected, very similar to that obtained from the fitting procedure. In this way, our In-Field Mössbauer data probably indicates a strongly correlation among the magnetic phases, with the sublattices of ferrite and those of AFM phase being strongly coupled and mostly aligned parallel and

antiparallel to the applied field direction. Another interesting feature concerning the dependence of the $B_{eff}$ of these sites with the applied field is observed, with a non-linear dependence. Specifically, for $H_{app}$ < 120 kOe, both sextets present a linear dependence but with angular coefficient of 0.8, lower than the expected for a perfect alignment (about 1), with $B_{eff}$ at $H_{app}$ = 120 kOe being the expected for a perfect alignment. Therefore, this effect probably indicates a canting of these lattices probably related to a spin-glass-like in the AFM phase or in the interface layer of the core/shell nanostructure[44]. Moreover, the angles between the Fe magnetic moment and the external magnetic field (θ, displayed in Table 2) can be calculated from the D12 parameter[50], and these angles corroborate with this argument. The third sextet with lower area and $B_{eff}$ is probably also related to a spin-glass-like magnetic structure in the AFM phase or in the interface between the magnetic phases.

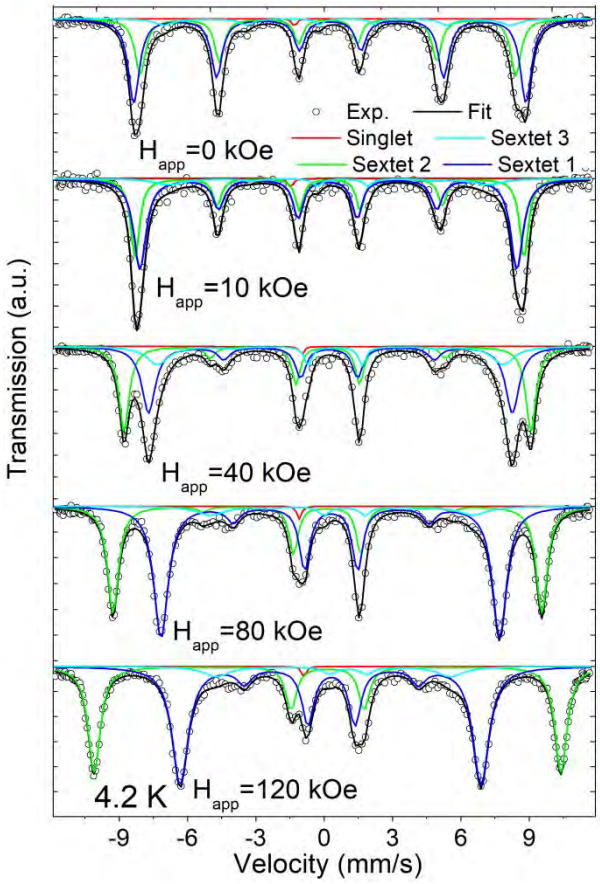


Figure 7 – In-Field Mossbauer Spectra of sample z=0.10 collected at 4.2 K with applied field up to 120 kOe. All the spectra were fitted with three sextets (Sextet 1 – blue, Sextet 2 - green and Sextet 3 – light blue) and a singlet (red).

Table 2 – Hyperfine Parameters obtained from the fitting procedure of the In-field Mössbuer spectra at 4.2 K: $H_{app}$ is the applied field, $B_{eff}$ is the effective field, IS is the Isomer Shift, QS is the quadrupolar splitting, W is the line width, dW is a parameter related with the width of each line of the sextets, D21 is the relation between the intensities of the lines 1 and 2, and the Area is the relative absorption area of each component.

| $H_{app}$ (kOe) | Subspectra | $B_{eff}$ (T) | IS (mm/s) | QS (mm/s) | W (mm/s) | dW | D21 | Θ degree | Area (%) |
|---|---|---|---|---|---|---|---|---|---|
| 120 | Sextet 1 | 63.4 | 0.28 | -0.01 | 0.55 | 0.59 | 0 | 0 | 35.4 |
| | Sextet 2 | 40.9 | 0.43 | -0.04 | 0.60 | 1.60 | 0.12 | 156 | 56.7 |
| | Singlet | - | -0.89 | - | 0.23 | - | - | | 0.5 |
| | Sextet 3 | 31.8 | 0.87 | -0.64 | 0.59 | 5.00 | 0 | 0 | 7.4 |
| 80 | Sextet 1 | 58.3 | 0.27 | 0.01 | 0.44 | 0.93 | 0.04 | 14 | 35.1 |
| | Sextet 2 | 46.0 | 0.42 | -0.04 | 0.52 | 1.39 | 0.10 | 158 | 56.2 |
| | Singlet | - | -0.97 | - | 0.23 | - | - | - | 0.6 |
| | Sextet 3 | 35.7 | 0.97 | -0.11 | 0.38 | 7.07 | 0.12 | 24 | 8.1 |
| 40 | Sextet 1 | 55.3 | 0.29 | -0.02 | 0.41 | 0.81 | 0.12 | 24 | 30.5 |
| | Sextet 2 | 49.4 | 0.38 | 0.06 | 0.53 | 1.19 | 0.17 | 152 | 48.9 |
| | Singlet | - | -0.85 | - | 0.23 | | - | - | 0.6 |
| | Sextet 3 | 47.0 | 0.51 | -0.21 | 0.25 | 5.56 | 0.07 | 18 | 20.0 |
| 10 | Sextet 1 | 52.8 | 0.37 | 0.00 | 0.40 | 0.37 | 0.33 | 39 | 35.1 |
| | Sextet 2 | 51.2 | 0.30 | 0.03 | 0.52 | 0.84 | 0.30 | 143 | 56.2 |
| | Singlet | - | -1.33 | - | 0.23 | | - | - | 0.6 |
| | Sextet 3 | 43.4 | 0.63 | -0.65 | 0.25 | 7.90 | 0.21 | 31 | 8.1 |
| 0 | Sextet 1 | 51.1 | 0.30 | 0.00 | 0.42 | 0.77 | 0.69 | - | 35.5 |
| | Sextet 2 | 53.3 | 0.39 | -0.01 | 0.56 | 0.15 | 0.69 | - | 56.7 |
| | Singlet | - | 0.19 | - | 0.7 | | - | - | 0.5 |
| | Sextet 3 | 47.1 | 0.92 | -0.42 | 0.25 | 4.61 | 0.69 | - | 7.3 |

## CONCLUSIONS

The synthesis of Zn-incorporated iron-oxide core-shell bimagnetic nanoparticles presented in this work represents a novel approach to the control of their magnetic properties by a chemically-tunable, magnetically coupled ferrimagnetic shell. The formation of an AFM $Fe_{1-y}O$ core strongly coupled to the FiM ferrite shell can be simply obtained from a standard one-pot thermal decomposition synthesis from $Fe(acac)_3$ and $Zn(acac)_2$ precursors. Compositional analysis by PIXE indicates that the Zn incorporation in the particle is lower than the nominal value of the synthesis, at the same time the compositional analysis by EELS indicates that the Zn is incorporated almost homogeneously in the whole particle, including the core and the shell. This result is interesting concerning the formation of the nanostructure, indicating the low solubility of the Zn ion in the AFM Wüstite phase (core), followed by the surface oxidation leading to the formation of the FiM ferrite phase at the shell, keeping the Zn/Fe relation along the whole nanoparticle. The incorporation of the Zn allows modified the overall magnetic properties of the MNPs. The effective anisotropy of the shell decreases with increasing the Zn amount, at the same time the AFM ordering of the core leads to an increment in the anisotropy of the whole system below $T_N$. No significant change in the $T_N$ of the AFM phase was observed with the limited incorporation of the Zn. Finally, a strong magnetic coupling between both phases is evidenced by the presence of the exchange bias field, with a canting of the spins observed with increasing the Zn amount in the system.

## Acknowledgments

The authors are thankful to the Argentinian Agency ANPCyT for the financial support through the grants PICT 2016-0288, PICT 2015-0118 and PICT 2014-2612. This work was partially supported by FAPESP – Sao Paulo Research Foundation (Brazil, Grant number 2016/21371-5). LCCMN is CNPq Fellows under Grants 305.647/2015-6. The authors also acknowledge the European Community's financial support under the RISE H2020-MSCARISE- 2016, SPICOLOST project.

## References

[1] Sun, S.; Zeng, H. Size-Controlled Synthesis of Magnetite Nanoparticles. *J. Am. Chem. Soc.* **2002**, *124*, 8204-8205.

[2] Sun S.; Zeng, H.; Robinson, D. B.; Raoux, S.; Rice, P. M.; Wang, S. X.; Li, G. Monodisperse MFe2O4 (M = Fe, Co, Mn) Nanoparticles. *J. Am. Chem. Soc.* **2004,** *126*, 273-279.

[3] Park, J.; An, K.; Hwang, Y.; Park, J. -G.; Noh, H. -J.; Kim., J. -Y.; Park, J. -H.; Hwang, N. -M.; Hyeon, T. Ultra-large-scale Syntheses of Monodisperse Nanocrystals. *Nature Materials* **2004,** *3*, 891-895.

[4] Lee, Y.; Lee, J.; Bae, C. J.; Park, J. G.; Noh, H. J.; Park, J. H.; Hyeon, T. Large-Scale Synthesis of Uniform and Crystalline Magnetite Nanoparticles Using Reverse Micelles as Nanoreactors under Reflux Conditions. *Adv. Funct. Mater.* **2005**, *15*, 503-509.

[5] Tavakoli, A.; Sohrabi, M.; Kargari, A. A Review of Methods for Synthesis of Nanostructured Metals with Emphasis on Iron Compounds. *Chem. Pap.* **2007,** *61*, 151-170.

[6] Kwon, S. G.; Hyeon, T. Formation Mechanisms of Uniform Nanocrystals via Hot-Injection and Heat-Up Methods. *Small* **2011**, *7*, 2685-2702.

[7] Frey, N. A.; Peng, S.; Cheng, K.; Sun, S. Magnetic Nanoparticles: Synthesis, Functionalization and Applications in Bioimaging and Magnetic Energy Storage. *Chem. Soc. Rev.* **2009,** *38*, 2532-2542.

[8] Roca, A. G.; Morales, M. P.; O'Grady, K.; Serna, C. J. Structural and Magnetic Properties of Uniform Magnetite Nanoparticles Prepared by High Temperature Decomposition of Organic Precursors. *Nanotechnol.* **2006**, *17*, 2783-2788.

[9] Roca, A. G.; Marco, J. F.; Morales, M. D. P.; Serna, C. J. Effect of Nature and Particle Size on Properties of Uniform Magnetite and Maghemite Nanoparticles. *J. Chem. Phys. C* **2007**, *111*, 18577-18584.

[10] Vargas, J. M.; Zysler, R. D. Tailoring the Size in Colloidal Iron Oxide Magnetic Nanoparticles. *Nanotechnol.* **2005**, *16*, 1474-1476.

[11] Lima Jr., E.; De Biasi, E.; Mansilla, M. V.; Saleta, M. E.; Effenberg, F., Rossi, L. M; Cohen, R.; Rechenberg, H. R.; Zysler, R. D. Surface Effects in the Magnetic Properties of Crystalline 3 nm Ferrite Nanoparticles Chemically Synthesized. *J. Appl. Phys.* **2010,** *108*, 103919.

[12] Arelaro, A. D.; Lima Jr., E.; Rossi, L. M.; Kiyohara, P. K.; Rechenberg, H. R. Ion Dependence of Magnetic Anisotropy in MFe2O4 (M=Fe, Co, Mn) Nanoparticles Synthesized by High-temperature Reaction. *J. Mag. Mag. Mater.* **2008,** *320*, e335-e338.

[13] Hou, Y.; Xu, Z.; Sun, S. Controlled Synthesis and Chemical Conversions of FeO Nanoparticles. *Angewandte Chemie Int. Ed.*, **2007**, *46*, 6329-6332.

[14] McCammon. C. A. Magnetic properties of FexO (x > 0.95): Variation of Neel Temperature. *J. Mag. Mag. Mater.* **1992**, *104*, 1937-1938.

[15] Lak, A.; Cassani, M.; Mai, B. T.; Winckelmans, N.; Cabrera, D.; Sadrollahi, E.; Marras, S.; Remmer, H.; Fiorito, S.; Cremades-Jimeno, L. et al. Fe2+ Deficiencies, FeO Sub-Domains, and Structural Defects Favor Magnetic Hyperthermia Performance of Iron Oxide Nanocubes into Intracellular Environment. *NanoLett.* **2018**, *18*, 6856-6866.

[16] Khurshid, H.; Li., W.; Chandra, S.; Phan, M.-H.; Hadjipanayis, G. C.; Mukherjee, P.; Srikanth, H. Mechanism and Controlled Growth of Shape and Size Variant Core/Shell FeO/$Fe_3O_4$ Nanoparticles. *Nanoscale* **2013**, *5*, 7942-7952.

[17] Unni, M.; Uhl., A. M.; Savliwala, S.; Savitzky, B. H.; Dhavalikar, R.; Garraud, N.; Arnold, D. P.; Kourkoutis, L. F.; Andrew, J. S.; Rinaldi, C. Thermal Decomposition Synthesis of Iron Oxide Nanoparticles with Diminished Magnetic Dead Layer by Controlled Addition of Oxygen. *ACS Nano* **2017**, *11*, 2284-2303.

[18] Kamzin, A. S.; Valiullin, A. A.; Khurshid, H.; Nemati, Z.; Srikanth, H.; Phan, M. H. Mössbauer Studies of Core–Shell FeO/Fe3O4 Nanoparticles. *Phys. Solid State* **2018,** *60*, 382-389.

[19] Sharma, S. K.; Vargas, J. M.; Pirota, K. R.; Kumar, S.; Leec, C. G.; Knobel, M. Synthesis and Ageing Effect in FeO Nanoparticles: Transformation to Core–Shell FeO/Fe3O4 and their Magnetic Characterization. *J. Alloy Comp.* **2011**, *509*, 6414-6417.

[20] Chen, R.; Christiansen, M. G.; Sourakov, A.; Mohr, A.; Matsumoto, Y.; Okada, S.; Jasanoff, A.; Anikeeva, P. "High-Performance Ferrite Nanoparticles through Nonaqueous Redox Phase Tuning" *Nanolett.* **2016**, *16*, 1345–1351.

[21] Vasilakaki, M.; Trohidou, K. N.; Nogués, J. Enhanced Magnetic Properties in Antiferromagnetic-Core/Ferrimagnetic-Shell Nanoparticles. *Sci. Rep.* **2015**, *5*, 9609.

[22] Lavorato, G.; Winkler, E. L.; Ghirri, A.; Lima Jr., E; Peddis, D.; Troiani, H. E.; Fiorani, D.; Agostinelli, E.; Rinaldi, D.; Zysler, R. D. Exchange Bias and Surface Effects in

Bimagnetic CoO−Core/$Co_{0.5}Ni_{0.5}Fe_2O_4$-Shell Nanoparticles. *Phys. Rev. B* **2016**, *94*, 054432.

[23] Lavorato, G. C.; Lima Jr., E.; Troiani, H. E.; Zysler, R. D.; Winkler, E. L. Tuning the Coercivity and Exchange Bias by Controlling the Interface Coupling in Bimagnetic Core/Shell Nanoparticles. *Nanoscale* **2017**, *9*, 10240-10247.

[24] Sun, X.; Huls, N. F.; Sigdel, A.; Sun, S. Tuning Exchange Bias in Core/Shell FeO/Fe3O4 Nanoparticles. *Nano Lett.* **2012**, *12*, 246-251.

[25] Kavich., D. W. ; Dickerson, J. H.; Mahajan, S. V.; Hasan, S. A.; Park, J.-H. Exchange Bias of Singly Inverted FeO/Fe3O4 Core-Shell Nanocrystals. *Phys. Rev. B* **2008,** *78*, 174414.

[26] Leszczyński, B.; Hadjipanayis, G. C.; El-Gendy, A. A.; Załęski, K.; Sniadecki., Z.; Musiał, A.; Jarek, M.; Jurga, S.; Skumiel, A. The Influence of Oxidation Process on Exchange Bias in Egg-Shaped FeO/Fe3O4 Core/Shell Nanoparticles. *J. Mag. Mag. Mater*. **2016**, *416*, 269-274.

[27] Chen, C. J.; Chiang, R. K.; Kamali, S.; Wang, S. L. Synthesis and Controllable Oxidation of Monodisperse Cobalt-Doped Wüstite Nanoparticles and Their Core–Shell Stability and Exchange-Bias Stabilization. *Nanoscale* **2015**, *7*, 14332-14343.

[28] Davar, F.; Salavati-Niasari, M.; Mir, N., Saberyan, K.; Monemzadeh, M.; Ahmadi, E. Thermal Decomposition Route for Synthesis of Mn3O4 Nanoparticles in Presence of a Novel Precursor. *Polyhedron* **2010**, *29*, 1747-1753.

[29] Chen, Q.; Rondinone, J. R.; Chakoumakos, B. C.; Zhang, Z. J. Synthesis of Superparamagnetic MgFe2O4 Nanoparticles by Coprecipitation. *J. Magn. Magn. Mater*. **1998**, *194*, 1-7.

[30] Liu, C.; Zou, B.; Rondinone, A. J.; Zhang, Z. J. Chemical Control of Superparamagnetic Properties of Magnesium and Cobalt Spinel Ferrite Nanoparticles through Atomic Level Magnetic Couplings. *J. Am. Chem. Soc.* **2000**, *122*, 6263-6267.

[31] Carter, R. E. "Thermal Expansion of MgFe,O, FeO, and MgO.2FeO. *J. Am. Ceram. Soc*. **1959**, *42*, 324-327.

[32] Hansson, R.; Hayes, P. C.; Jak, E. In *Phase Equilibria in the Fe-Zn-O System at Conditions Relevant to Zinc Sintering and Smelting*. Proceedings of VII International Conference on Molten Slags Fluxes and Salts, The South African Institute of Mining and Metallurgy, 2004, 209.

[33] Kmita, A.; Pribulova, A.; Holtzer, M.; Futas, P.; Roczniak, A. Use of Specific Properties of Zinc Ferrite in Innovative Technologies. *Arch. Metall. Mater.* **2016**, *61*, 2141–2146.

[34] Anooj, E. S.; Sreelekshmi, S. J.; Gopukumar, S. T.; Praseetha, P. K. Evaluation of the Zinc Ferrite Nano particles for Bio-applications. *Int. J. Pharm. Sci. Rev. Res.* **2017**, *46*, 22-26.

[35] Hanini, A.; Lartigue, L.; Gavard, J.; Kacem, K.; Wilhelm, C.; Gazeau, F.; Chau, F.; Ammar, S. Zinc Substituted Ferrite Nanoparticles with Zn0.9Fe2.1O4 Formula Used as Heating Agents for in vitro Hyperthermia Assay on Glioma cells. *J. Magn. Magn. Mater.* **2016**, *416*, 315-320.

[36] Yang, Y.; Liu, X.; Yang, Y.; Xiao, W.; Li, Z.; Xue, D.; Li, F.; Ding, J. Synthesis of Nonstoichiometric Zinc Ferrite Nanoparticles with Extraordinary Room Temperature Magnetism and Their Diverse Applications. *J. Mater. Chem. C* **2013**, *1*, 2875-2885.

[37] Johansson, S. A. E.; Campbell, J. L.; Malmqvist, K. G. *Particle-Induced X-ray Emission Spectrometry (PIXE)*. Wiley: Hoboken, USA, 1995.

[38] Limandri, S.; Olivares, C.; Rodriguez, L.; Bernardi, G.; Suárez, S. PIXE Facility at Centro Atomico Bariloche. *Nucl. Instr. Meth. Phys. Res. B* **2014**, *318*, 47-50.

[39] Campbell, J. L.; Boyd, N. I.; Grassi., N.; Bonnick., P.; Maxwell, J. A. The Guelph PIXE Software Package IV. *Nucl. Instr. Meth. Phys. Res. B* **2010,** *268*, 3356-3363.

[40] Lima Jr, E.; Winkler, E. L.; Tobia, D.; Troiani, H. E.; Zysler, R. D.; Agostinelli, E.; Fiorani, D. Bimagnetic CoO Core/CoFe2O4 Shell Nanoparticles: Synthesis and Magnetic Properties. *Chem. Mater.* **2012**, *24*, 512-516.

[41] Dormann, J. L.; Fiorani, D.; Tronc, E. Magnetic Relaxation in Fine-Particle Systems. *Adv. Chem. Phys.* **1997**, *98*, 283-494.

[42] Smit, J.; Wijn, H. P. J. *Ferrites: Physical Properties of Ferrimagnetic Oxides in Relation to Their Technical Applications*. Philips Technical Library: Eindhoven, Netherland, 1959.

[43] Chinnasamy, C. N.; Narayanasamy, A.; Ponpandian, N.; Chattopadhyay, K.; Guerault, H.; Greneche; J. M. Magnetic Properties of Nanostructured Ferrimagnetic Zinc Ferrite. *J. Phys.: Condens. Matter* **2000**, *12*, 7795-7805.

[44] Pandey, B.; Litterst, F. J.; Baggio-Saitovitch, E. M. Preferential Spin Canting in Nanosize Zinc Ferrite. *J. Mag. Mag. Mater.* **2015,** *385*, 412-417.

[45] Morrish, A. H.; Clark, P. E. High-Field Mossbauer Study of Manganese-Zinc Ferrites. *Phys. Rev. B* **1975,** *11*, 278-286.

[46] Trohidou, K.; Vasilakak, M. Monte Carlo Studies of Magnetic Nanoparticles. In: *Applications of Monte Carlo Method in Science and Engineering*. Mordechai S., Ed., IntechOpen, 2011; Chap. 20, 513-538.

[47] Estrader, M.; López-Ortega, A.; Golosovsky, I. V.; Estradé, S.; Roca, A. G.; Salazar-Alvarez, G.; López-Conesa, L.; Tobia, D.; Winkler, E.; Ardisson, J. D. et al. Origin of the Large Dispersion of Magnetic Properties in Nanostructured Oxides: FexO/Fe3O4 Nanoparticles as a Case Study. *Nanoscale* **2015**, *7*, 3002-3015.

[48] Checherskaya, L. F.; Romanov, V. P.; Tatsienko, P. A. Mossbauer Effect in Wustite. *Phys. Stat. Sol. a* **1973**, *19*, K177-K182.

[49] Lima Jr., E.; Brandl, A. L.; Arelaro, A. D.; Goya, G. F. "Spin Disorder and Magnetic Anisotropy in Fe3O4 Nanoparticles. *J. Appl. Phys.* **2005,** *99*, 083908.

[50] Pianciola, B. N.; Lima Jr., E.; Troiani, H. E.; Nagamine, L. C. C. M.; Cohen, R.; Zysler, R. D. Size and Surface Effects in the Magnetic Order of the CoFe2O4 Nanoparticles. *J. Magn. Magn. Mater.* **2015**, *377*, 44-51.

TOC Graphic

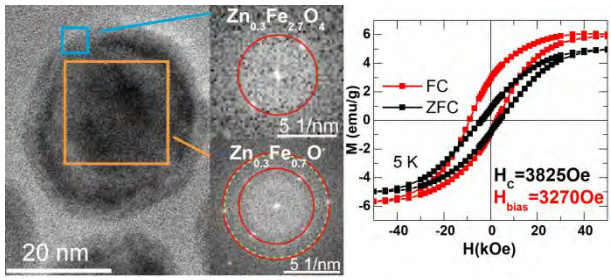
Zn0.3Fe2.7O4
5 1/nm
Zn0.3Fe2.7O4
20 nm
5 1/nm
FC
ZFC
5 K
Hc=3825Oe
Hbias=3270Oe
M (emu/g)
H(kOe)

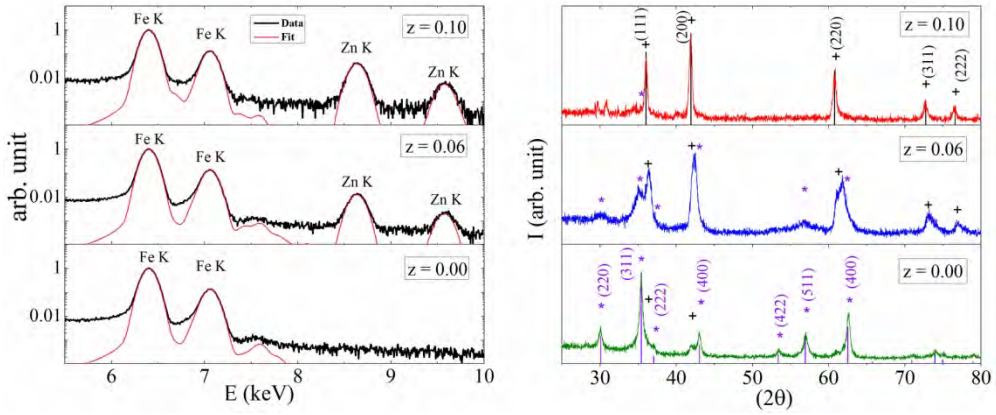


Figure 1 – Left Panel: PIXE spectra of all samples showing the pertinent energy range of Fe and Zn K-peaks. Black lines correspond to experimental data, and red lines are the respective fitting to obtain the z =[Zn]/[Fe] ratio for each system. Right panel: XRD profiles of three samples. All peaks are indexed with the Fe1-yO (+) and ferrite (*) phases where the bars correspond to the diffraction peaks according to the JCPDS card number: for Wüstite 00-006-0615 (upper panel) and magnetite 00-019-0629 (bottom panel).

159x66mm (300 x 300 DPI)

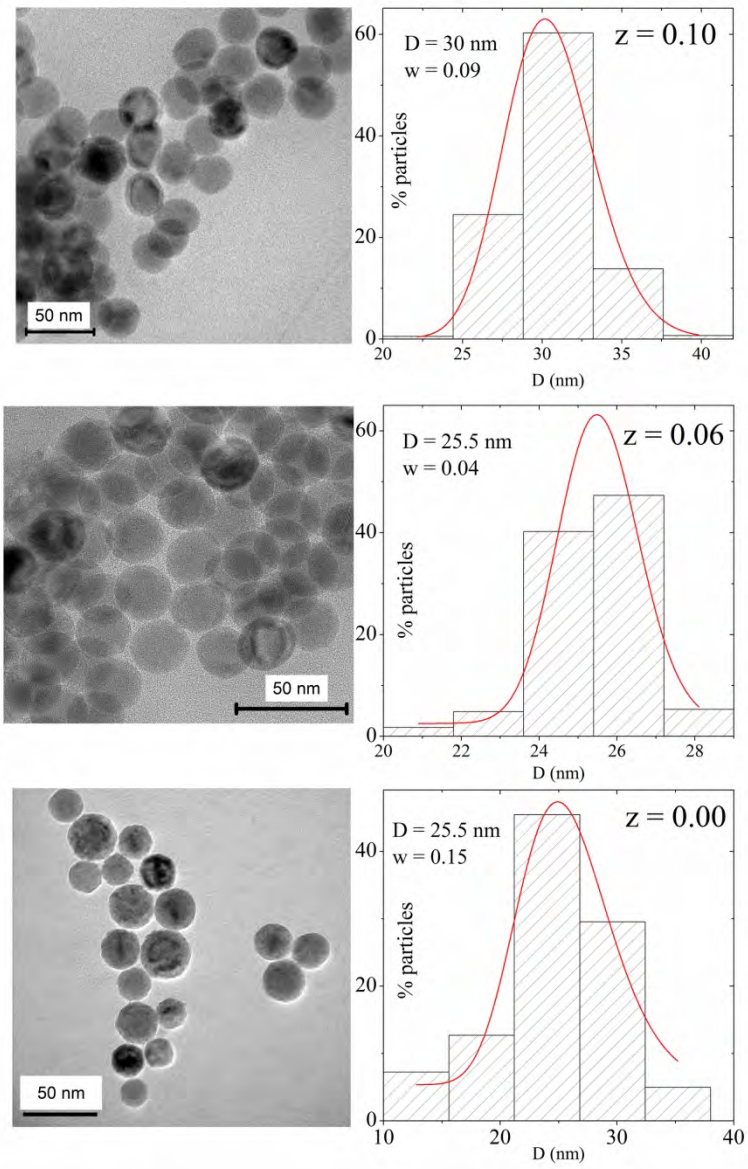


Figure 2 – Representative TEM image for each sample with the corresponding histogram of diameters obtained with measuring more than 300 particles. Each histogram is fitted with a lognormal distribution in order to obtain the mean diameter and the dispersion.

159x239mm (300 x 300 DPI)

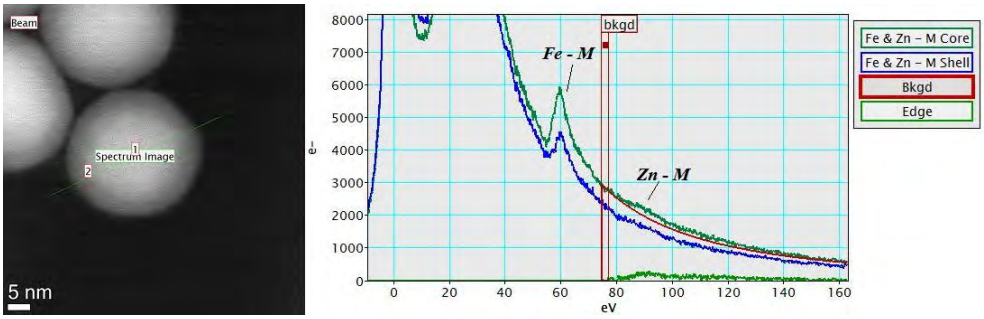


Figure 4 - STEM-HAADF image of nanoparticles of sample z = 0.10 (left) and low-loss EEL spectra (right) at different positions of the nanoparticle (indicated by 1 and 2 in the figure). The Fe-M and Zn-M edges are indicated. Background subtracted is indicated (red line). The background subtracted Zn-M edge is also shown.

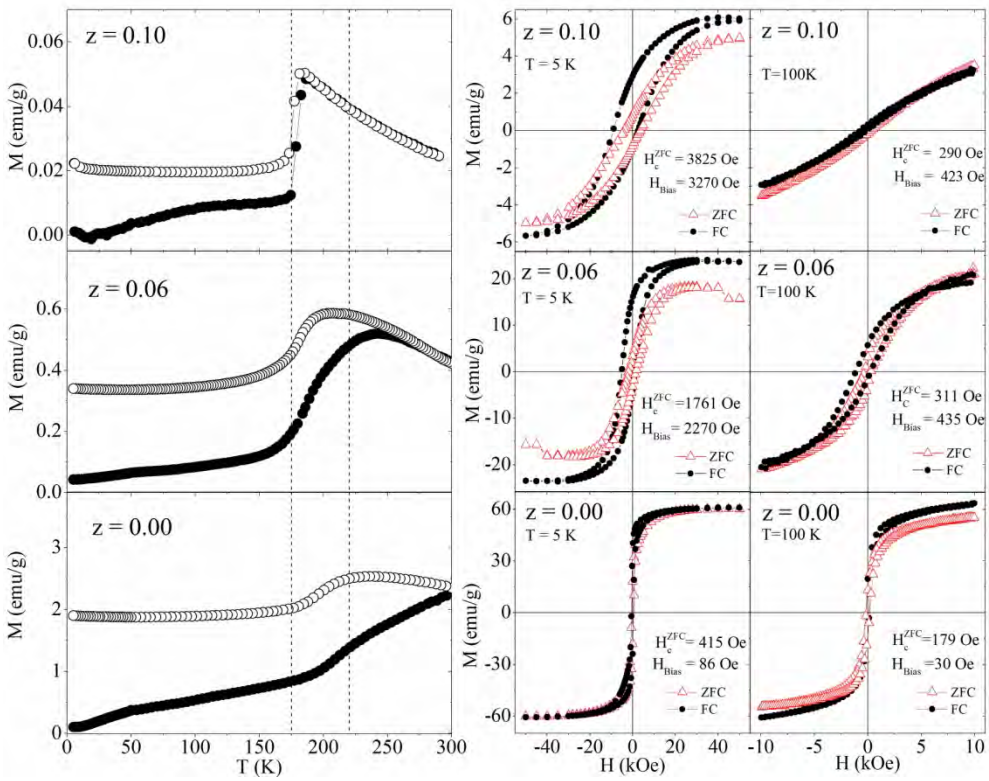


Figure 5 – Left panel: M(T) data of all samples measured in both ZFC (solid symbols) and FC (open symbols) protocols with HFC=50 Oe. Right panel: ZFC (open symbols) and FC (solid symbols) hysteresis loops measured at 5 K (left panels) and 100 K (right panels). The values of coercive fields after ZFC (HCZFC) and bias fields after FC defined as HBias=(HC+-HC-)/2) are also displayed.

159x124mm (300 x 300 DPI)

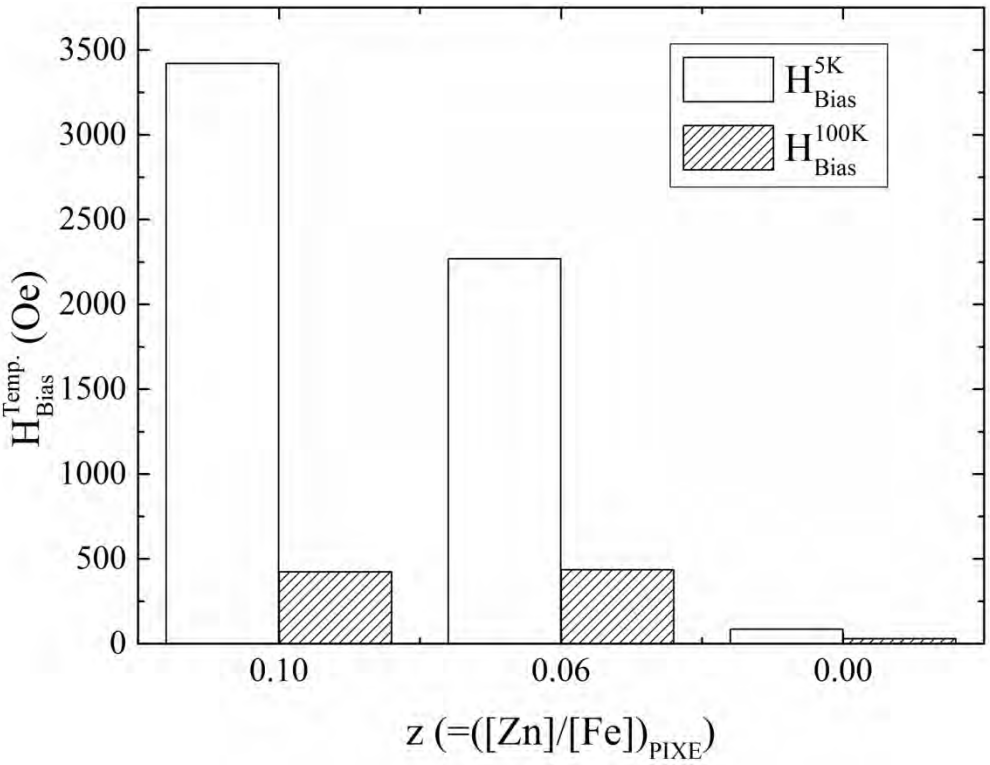


Figure 6 - Exchange bias field at 5 K (Hbias5K) and 100 K (Hbias100K) as a function of the Zn concentration of the sample obtained from PIXE analysis.

79x61mm (600 x 600 DPI)

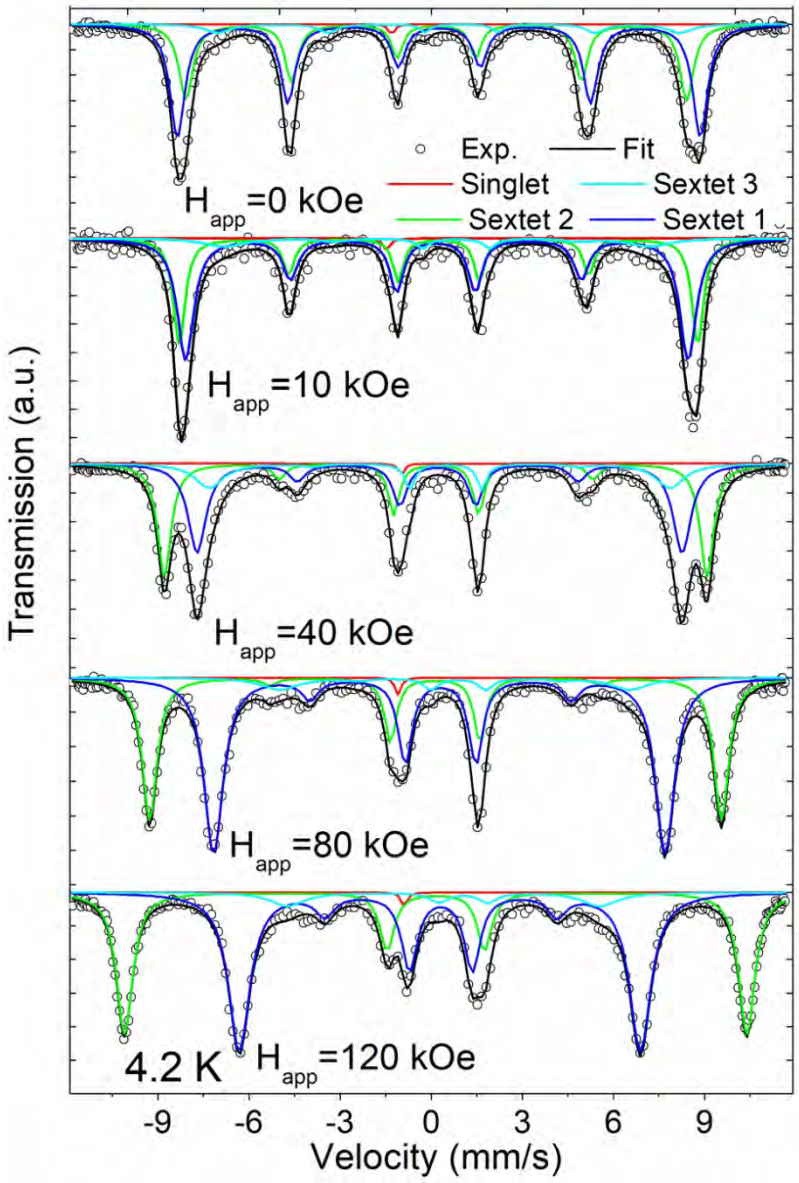


Figure 7 – In-Field Mossbauer Spectra of sample z=0.10 collected at 4.2 K with applied field up to 120 kOe. All the spectra were fitted with three sextets (Sextet 1 – blue, Sextet 2 - green and Sextet 3 – light blue) and a singlet (red).

79x118mm (300 x 300 DPI)